Optimizing DC-DC Converter Topologies for Enhanced Efficiency in Hybrid Renewable Energy Systems Using Hybrid Techniques

P. Veeramanikandan[1†], **Veena G N**[2],
R. Giri Prasad[3], and **Elangovan Muniyandy**[4,5], Non-members

ABSTRACT

In hybrid renewable energy systems (HRES), the use of DC-DC converter topologies is fundamental for enabling efficient energy source utilization and significantly enhancing overall power efficiency. However, the complexity of designing and implementing various DC-DC converter topologies can lead to increased costs and maintenance challenges in HRES. This paper proposes a hybrid method for optimizing DC-DC converters in HRES to enhance power efficiency. The ARO is used to optimize the converter design parameters. The PHNN is used to predict these optimized parameters. By then, the recommended method is implemented in the MATLAB platform, and they evaluate their performance with various existing methods such as Jellyfish Search and Random Decision Forest (JS-RDF), Improved Non-Dominated Sorting Genetics (INSGA-II), Earthquake Optimization Algorithm (EA), Particle Swarm Optimization and Lightning Attachment Procedure Optimization (PSO-LAPO), and Galactic Swarm Optimization (GSO). The proposed ARO-PHNN method demonstrates exceptional performance with an efficiency of 98.1%. In terms of statistical analysis, it exhibits a mean value of 0.9421 and a median of 0.8612, reflecting its high accuracy. Additionally, the method has a low standard deviation (SD) of 0.0065, indicating not only superior performance but also enhanced stability and consistency compared to other techniques.

Keywords: Hybrid Renewable Energy Systems, DC-DC Converter Topologies, ARO, PHNN, PSO, Jellyfish Search

1. INTRODUCTION

(a) Background

HRES emerged because of RES advancement to handle greenhouse effects while reducing fossil fuel usage, therefore integrating numerous power sources consisting of solar and wind power together with energy reserves [1, 2]. Power system efficiency depends heavily on DC-DC converters since they regulate power distributions and maximize extraction capabilities from different energy sources [3, 4]. The implementation of buck, boost, buck-boost converters, and advanced multi-input as well as bi-directional converters enables systems to operate successfully under dynamic renewable generation conditions [5, 6]. These topologies operate to optimize voltage levels together with enhancing energy conversion efficiency while improving system stability and reliability according to [7, 8]. The increasing need for sustainable energy requires advanced knowledge of innovative DC-DC converter topology implementation to achieve maximum benefits from HRES systems [9, 10]. A thorough study of basic principles combined with benefits and technical hurdles in different DC-DC converter designs reveals their capability to improve both power efficiency and HRES utilization [11-13]. Power transfer control and loss-minimizing strategies implemented by these converters enhance energy production and power loss reduction while enabling effortless power connections between various energy sources and storage units to advance high- efficiency, low-carbon energy systems [14, 15].

(b) Challenges

The adoption of DC-DC converters in HRES systems faces ongoing technological barriers for their best possible utilization. The integration of RES such as solar and wind power presents control difficulties because their variable inputs cause unstable voltage and power output conditions. The development of converters for multi-source systems becomes more complex when each source demonstrates different electrical characteristics since it usually needs advanced control methods for operation. The system performance experiences significant deterioration because of efficiency losses that occur mostly when the system operates under partial load conditions. Efficient thermal management becomes necessary because high-power converters produce sub-

Manuscript received on November 29, 2024; revised on February 9, 2025; accepted on March 23, 2025. This paper was recommended by Associate Editor Chainarin Ekkaravarodome.

[1]The author is with Dhanalakshmi Srinivasan college of Engineering and Technology, Chennai, India.

[2]The author is with REVA University, Karnataka, India.

[3]The author is with Aditya University, Andhra Pradesh, India.

[4]The author is with Saveetha Institute of Medical and Technical Sciences, Chennai, India.

[5]The author is with Applied Science Private University, Amman, Jordan.

[†]Corresponding author: p23veeramanikandan@gmail.com

Digital Object Identifier: 10.37936/ecti-eec.2525232.256882

stantial heat, which can affect reliability unless suitable measures are implemented. Achieving compactness and cost-effectiveness while maintaining high efficiency, reliability, and scalability remains a key engineering challenge. The integration of energy storage and bidirectional power flows introduces more complexities, necessitating robust and adaptive converter designs to ensure long-term system stability and efficiency.

(c) Literature Survey

Previous research has explored various techniques and aspects for DC-DC topology. Some of these studies are reviewed below.

For HRES, Karthikeyan and Jebaselvi [16] introduced a hybrid strategy that makes use of a 4-port DC–DC converter that can function both independently and in tandem with the grid. The suggested method's main objectives were to guarantee consistent voltage profiles, improve system performance, and lower power losses. The RDF uses machine learning to forecast the best control pulses, increasing overall efficiency, while the JS was utilized for robust optimization, adjusting the converter to different conditions. Hasanpour et al. [17] presented a revolutionary non-isolated, high-gain, high-efficiency interleaved DC-DC converter with low voltage stress that was appropriate for applications involving RES. It achieves an ultra-step-up voltage ratio by using a built-in transformer (BIT) and a coupled inductor (CI). In this situation, the CI and BIT turn ratios offered a more adaptable voltage gain. Equal current sharing performance across the interleaved phases was achieved, and the input current ripple was reduced thanks to the interleaving effect. Furthermore, lowering the voltage stress across, which in turn lowers the conduction losses, made it easier to develop low-voltage MOSFETs. In isolated step-up DC–DC converters, Meshael et al. [18] have shown how to offer soft switching by utilizing passive and active snubbers. Additionally, the 3 most popular boost approaches were thoroughly examined. This approach led to a decrease in both the turn ratio and the voltage stress.

For electric vehicle (EV) battery charging applications, this study recommends a photovoltaic (PV) integrated DC to DC enhancing converter at the front ends of the current DC–DC converter methodology, even though Rajasekaran et al. [19] introduced an MPPT and the INSGA-II algorithm to achieve constant switching with design optimization. The modified SEPIC converter and MPPT-based NSGA-II approaches were combined to create an effort that would enhance the system's overall performance. Mendez-Flores et al. [20] have presented a range of well-researched optimization techniques to maximize the energy harvested under different environmental conditions and to maximize the effectiveness of the required power electronics for the execution of MPPT algorithms. Two methods for the best proportional integral-derivative (PID) controllers in an HRES have been presented by Saleh et al. [21]. These methods were LAPO and PSO. Using DC/DC boost converters, a PV source, wind turbine (WT), and battery storage were connected to a point of common coupling in this study's HRES. A voltage source controller and a current controller make up the inverter's controller, which produces 3 PID gains at each controller. A time domain objective function was developed using the voltage and current faults to determine the PID gains. Rajasekaran and Rani [22] demonstrated how to apply an EM control approach based on closed-loop proportional-integral (PI) with the goal to address and evaluate the problems of unstable DC link voltage. When in grid-connected mode, a hybrid energy storage system made up of battery units and a supercapacitor was charged utilizing a variety of hybrid energy sources, including solar and wind. The main objective of this effort was to provide energy storage units (supercapacitors and batteries) to the grid in case solar or wind energy sources were unavailable. The combined creation of a GSO-based incremental conductance technique is used to analyze the maximum power that this suggested system was able to track.

(d) Research Gap and Motivation

Despite the extensive exploration of optimization techniques such as JS-RDF, INSGA-II, EA, PSO, LAPO, and GSO across various RES, key gaps remain. First, many of these techniques primarily target isolated system performance improvements, such as reducing power losses or enhancing voltage stability, but do not effectively address the complex, multi-objective trade-offs required in HRES that integrate both energy storage and multiple generation sources. Furthermore, validation of these algorithms, especially under varying environmental and grid-connected conditions, is sparse. In particular, techniques like EA and JS-RDF, while theoretically promising for control pulse prediction and system adaptation, have not been comprehensively tested for performance in rapidly fluctuating renewable environments. Additionally, the potential synergies of hybridizing these methods to leverage their individual strengths for enhanced scalability and robustness in multi-port converter architectures are underexplored. Addressing these gaps could significantly improve the operational reliability and efficiency of HRES. The aforementioned disadvantages are motivated to do this work.

(e) Contribution

The following is a summary of this paper's main contributions:

- The ARO-PHNN method significantly improves the efficiency of DC-DC converters in HRES, leading to better energy utilization.
- By employing ARO, the method effectively optimizes the design parameters of converters, enhancing their overall performance.
- The integration of PHNN allows for accurate predictions of optimized parameters, improving the system's

responsiveness and reliability.
- The proposed method exhibits superior stability and consistency in performance compared to traditional optimization techniques, contributing to more reliable EM.
- The method undergoes thorough testing against various existing optimization techniques, demonstrating its advantages and effectiveness in HRES.

(f) Novelty

The innovative ARO-PHNN suggested method merges ARO technology with PHNN optimization to provide optimized DC-DC converters for HRES applications. Through this combined methodology, operators enhance power conversion performance while reducing difficulties found in different converter designs. ARO-PHNN unites both optimization techniques to create an advanced method that obtains outstanding prediction accuracy through stable performance. This comprehensive framework not only improves EM but also offers a robust solution to the challenges of cost and maintenance in HRES, setting a new standard for future research and application in this field.

(g) Organization

The paper's remaining section is arranged as follows: Part 2 describes the configuration of the DC-DC converter in HRES. Part 3 illustrates the proposed hybrid ARO-PHNN method. The results and discussion are presented in Part 4. The manuscript is concluded in Part 5.

2. CONFIGURATION OF DC-DC CONVERTER TOPOLOGY IN HRES

Fig. 1 illustrates an HRES combining solar PV and wind energy sources. The solar PV is connected to a DC-DC converter, while the WT is linked to an AC-DC converter. The battery is also connected to the DC-DC converter, allowing for energy storage and regulation [23]. The DC-AC converter manages the power flow between the wind energy and the grid. A proposed ARO-PHNN approach is applied to optimize the performance of the DC-DC converter, ultimately improving the efficiency of the overall system. The diagram demonstrates the integration and coordination of various energy sources with the grid.

2.1 Modelling of PV

The best design of a solar PV cell depends on modeling, which raises the PV system's overall performance. Any PV system's behavior in real time can be efficiently mirrored by a precise and comprehensive PV cell model. However, the cell's intrinsic nonlinearity makes modeling PV cells difficult [24]. The total current produced by the single-diode PV model is shown by the following expression:

$$i = i_{PV} - i_d - i_P \tag{1}$$

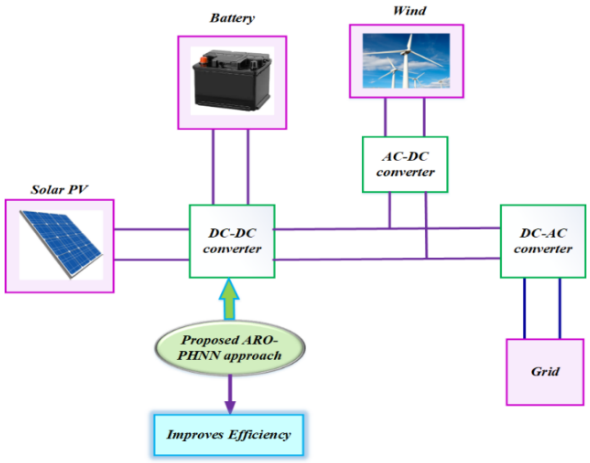

***Fig. 1**: Structure of a HRES featuring solar PV, wind energy, battery storage, and optimized DC-DC converters.*

where the current flowing through the diode is indicated by i_d, the current flowing through the PV by i_{PV}, and the current flowing through the shunt resistance by i_P. The current equation can be written as follows by substituting i_d and i_P:

$$i = i_{PV} - i_0 \left(EXP \left(\frac{V_d}{q_1 V_t} - 1 \right) \right) - \left(\frac{V + iR_S}{R_P} \right) \tag{2}$$

where i_0 stands for the diode, d for the diode leakage current, R_S for the number of cells connected in series, V_t for the thermal voltage, and q_1 for the ideality factor.

$$i_{PV} = \left(\frac{g}{g_0} \right) \left[i_{SC} + K_j \left(T - T_0 \right) \right] \tag{3}$$

The actual temperature and irradiation values are shown by g and T, respectively, while the current coefficient factors are represented by K_j. i_{SC} stands for the short-circuit current under standard test conditions. T and K stand for the cell temperature in Kelvin and the Boltzmann constant, respectively.

2.2 Modeling of Wind

A WT's power output is determined by the wind's velocity and the area it blows across [25]. One can compute the power derived by a WT as follows:

$$P_W(T) = \begin{cases} 0 & S(T) \le S_{cin} \text{ or } S(T) \ge S_{coff} \\ P_r^W \frac{S(T) - S_{cin}}{S_r - S_{cin}} & S_{cin} < S\ (T)\ < S_R \\ P_r^W & S_R \le S(T) < S_{coff} \end{cases} \tag{4}$$

where $St(T)$, P_r^W, S_{cin}, and S_r represent the wind speed (WS) at the required height, the rated power of WT, the rated WS, and the cut-in and cut-off speeds, respectively. An illustration of WS throughout the year is a probability density function (PDF), which is a curve.

$$P\left(s_1 \le s \le s_2\right) = \int_{s1}^{s2} F_s ds \tag{5}$$

***Table 1**: Performance parameter.*

Components	Parameter	Values
Battery	Rated Capacity	55 Ah
	Nominal Voltage	15 V
	Initial SoC	100 %
PV	Module	Sun Power SPR-305-WHT
	Number of series connected per string	20
	Count of parallel strings	35
WT	Base WS	8 m/s
	Base rotational speed	0.5 p.u
	Max. power at base WS	0.9 p.u
	Nominal mechanic output power	1500e9 (W)
	Base power of electric generator	1500e6/0.9 (VA)
PMSG	Stator phase inductance	8.5 e^{-3}
	Stator phase resistance	1.5 Ω
	Inertia	0.01197 J/kg.m^2
	Pole pairs	5

$$P\left(0 \leq s \leq \infty\right) = \int_{s1}^{\infty} F_s ds = 1 \tag{6}$$

where F_s represent the WS PDF, s_1 and s_2 represent any 2 WS. The waybill probability function is the most significant PDF in WS statistics. The definition of the waybill probability function, which serves as the foundation for describing WS statistics, is as follows:

$$F_s = \frac{K}{C}\left(\frac{s}{C}\right)^{K-1} \exp\left(\left(\frac{s}{C}\right)^{K}\right) \tag{7}$$

In this case, the shape parameter, scale parameter, and WS are represented, respectively, by K, C and s. The WS at a specific height may be found using the following formula:

$$S = S_0\left(\frac{E_W}{E_0}\right)^{\alpha} \tag{8}$$

where S, S_0 and α represent the WS at a required height E_W, E_0 represent the WS at reference height and the friction coefficient, respectively.

$$P_W\left(T\right) = M_W P_W\left(T\right) \tag{9}$$

where M_W represents the number of WT. Table 1 shows the performance parameter.

3. PROPOSED HYBRID ARO-PHNN METHOD FOR OPTIMIZING DC-DC CONVERTERS

The proposed hybrid ARO-PHNN method integrates ARO and PHNN to optimize DC-DC converters in HRES. It begins by initializing a population of rabbits, each representing potential design solutions, with their fitness evaluated based on energy performance criteria. Rabbits interact socially, sharing fitness information to adapt their positions in the solution space, thereby balancing exploration and exploitation. PHNN models the relationships between design parameters and performance outcomes, enhancing predictive accuracy. The detailed description of the proposed method is described as follows:

3.1 Artificial Rabbits Optimization

ARO is a nature-inspired optimization algorithm that mimics the hunting behavior and movement patterns of rabbits in a dynamic environment [26]. The algorithm utilizes a population of artificial rabbits that move through the solution space, with each rabbit representing a potential solution. These rabbits adjust their positions based on local and global best solutions, ensuring efficient exploration while avoiding premature convergence. The key advantages of ARO include its simplicity, adaptability to various optimization problems, and ability to handle complex and nonlinear systems. Additionally, ARO exhibits high convergence speed, robustness against local minima, and efficient computational performance, making it well-suited for optimizing parameters in DC-DC converter topologies and other engineering applications.

Step 1: Initialization

Set the initial values for the input parameters, including the WS, battery, and PV current and voltage.

Step 2: Random Generation

Following initialization, random vectors are used to create the input parameters at random.

Step 3: Fitness Function

$$F = Max\left(Efficiency\right) \tag{10}$$

Step 4: Exploration Phase

In ARO, rabbits exhibit "detour foraging," where they neglect nearby resources and randomly forage in other regions. Each rabbit updates its position by moving towards a randomly selected rabbit in the swarm, adding a perturbation to simulate this behavior. This model represents the collective search strategy in ARO.

$$\begin{aligned}\vec{U}_I(T+1) = \vec{Z}_J(T) + \\ S\left(\vec{Z}_I(T) - \vec{Z}_J(T) + R(0.5(0.05 + s_1))\right) \\ N_1, I, J = 1, ..., N \text{ and } J \neq I\end{aligned} \tag{11}$$

where $\vec{U_I}\left(T+1\right)$ represents the potential location of the Ith rabbit at time $T+1$, $\vec{Z_I}\left(T\right)$ represents the Ith rabbit's position at time T, N denotes the population size of rabbits, T is the maximum number of iterations, [.] denotes the ceiling function, and R denotes rounding to the closest integer. The parameter of ARO is presented

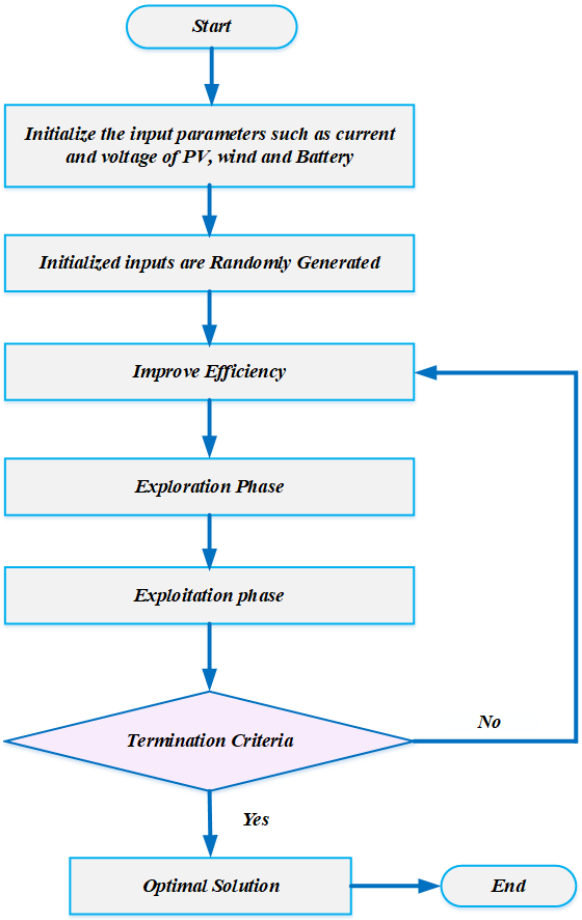

***Fig. 2**: Flowchart of ARO.*

***Table 2**: Parameter of ARO.*

Parameter	Value/Setting
Population Size	50
Maximum Function Evaluations	50,000
Number of Runs per Function	30

in Table 2.

Step 5: Exploitation Phase

In ARO, each rabbit creates multiple burrows around its position in the search space and randomly selects one for hiding at each iteration to avoid predators. This behavior reduces the likelihood of being preyed upon and is mathematically modeled.

$$\vec{C}_{I,J}(T) = \vec{Z}_I(T) + A \cdot B \cdot \vec{Z}_I(T), \quad I = 1,..,N \text{ and } J = 1,..,D \tag{12}$$

where D is the hidden parameter and A is the problem's dimension. Fig. 2 presents the flowchart of ARO.

Step 6: Termination

Check the termination criteria; proceed to step 3 if the optimal solution was not discovered. If it was, the procedure is over.

Computational complexity

A relevant metric for assessing an algorithm's effectiveness in solving optimization problems is computational complexity. The variable dimensionality of problems (d), the maximum number of iterations (T), and the number of participants (n) all affect complexity. ARO's total computational complexity can be expressed as

$$\begin{aligned} O(ARO) &= O(problem\,definition) + O(initialization) \\ &\quad + O(function\,Evaluation) \\ &\quad + O(Position\,Updating\,in\,\det our\,foraging) \\ &\quad + O(position\,updating\,in\,random\,hiding) \end{aligned} \tag{13}$$

$$= O\left(1 + n + Tn + \frac{1}{2}Tnd + \frac{1}{2}Tnd\right) \cong O(Tnd + Tn + n)$$

3.2 Pseudo-Hamiltonian Neural Networks

PHNN are a type of neural network designed to solve optimization problems by leveraging the principles of Hamiltonian mechanics [27]. These networks utilize an energy-based framework, where the network's state is represented as a dynamic system with energy functions that guide the optimization process. The PHNN algorithm models the optimization task as a process of energy minimization, with the network evolving towards an optimal configuration that corresponds to the minimal energy state. The primary advantage of PHNN lies in its ability to efficiently predict the optimized parameters by learning from data and adjusting the network weights dynamically. This approach enhances the accuracy and reliability of predictions, making it highly suitable for complex tasks like optimizing DC-DC converter parameters. PHNN offers key benefits such as fast convergence, high adaptability to various system complexities, and improved stability, ensuring more precise and effective optimization compared to traditional methods.

$$U = T(u)\Delta F(u) \tag{14}$$

For some skew-symmetric matrix $T(u) = -T(u)^t \in R^{d\times d}$.

$$\frac{dF}{dV} = \nabla F(u)J(u) = 0 \tag{15}$$

The matrix $T(u)$ is often not unique if $u > 2$, although it may depend on u.

$$u = (T(u) - X(u)\nabla F(u) + A(u,v) \tag{16}$$

where $X(u) \in R^{d\times d}$ and $(u)\,R\,(u)\,u \geq 0$ for all u.

$$(u,v) = (T - X)\nabla F(u) + A(u,v) \tag{17}$$

$$B = \left| \frac{u - u^e}{\Delta v} - \theta \right| \tag{18}$$

Given a single data point u, the last term represents the B-regularization of the external force.

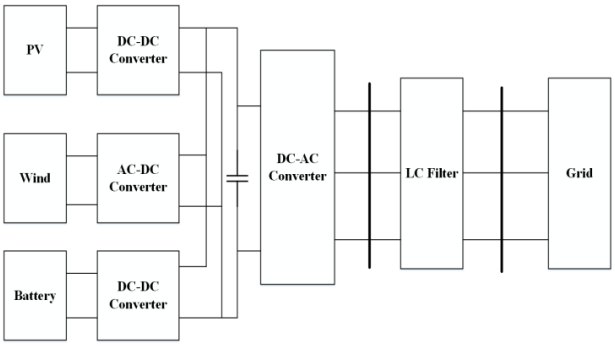

***Fig. 3**: Simulink Diagram.*

4. RESULTS AND DISCUSSION

The results of the application of the suggested hybrid optimization approach are shown in this part. The results highlight significant improvements in performance metrics, including efficiency, accuracy, and stability of the DC-DC converters optimized using the hybrid approach that integrates ARO and PHNN. The proposed ARO-PHNN method is compared with other approaches such as JS-RDF, INSGA-II, EA, PSO-LAPO, and GSO. Three distinct cases were analyzed: Cases 1 and 2 dealt with variations in irradiance in conjunction with a 3-phase load, and Case 3 dealt with variations in WS in conjunction with a 3-phase load failure. Fig. 3 illustrates the Simulink diagram.

MATLAB Version: 9.8.0.1451342 (R2020a)

Case 1: Variation in Irradiance

Fig. 4 shows the change in irradiance (measured in W/m^2) over time (in seconds) in Case 1. The irradiance starts at a high value of 1000 W/m² and remains constant for the first 0.2 seconds. After 0.2 seconds, there is a sharp drop to approximately 600 (W/m^2), followed by a further decline to about 500 (W/m^2) around 0.6 seconds. This lower irradiance level persists until about 1.0 seconds, after which it begins to rise sharply again, returning to the initial 1000 W/m² value by around 1.2 seconds. This plot represents the fluctuations in solar irradiance over time, which could be due to changes in sunlight conditions, such as passing clouds or other environmental factors. Fig. 5 shows the speed (in m/s) over time (in seconds) for Case 1. The speed remains constant at 12 m/s throughout the entire duration of 1.4 seconds, with no visible fluctuations or changes. This suggests that the system maintains a steady speed, possibly indicating stable wind conditions or a controlled environment where the speed is not affected by the changes in other variables, such as irradiance. Fig. 6 shows the power contributions of different sources over time. The PV power starts at approximately 3200 kW and fluctuates between 2800 kW and 3400 kW. The wind power quickly rises from 0 to about 3000 kW by 0.2 seconds and then stabilizes between 2500 kW and 2800 kW. The battery power spikes to around 5000 kW initially and then settles around 4500 kW with minor

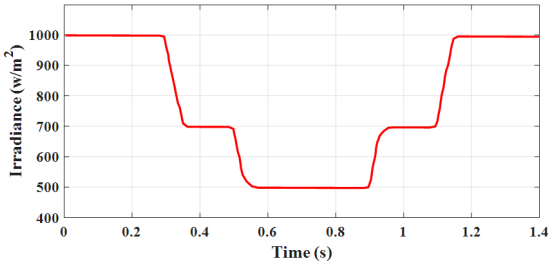

***Fig. 4**: Irradiance change analysis.*

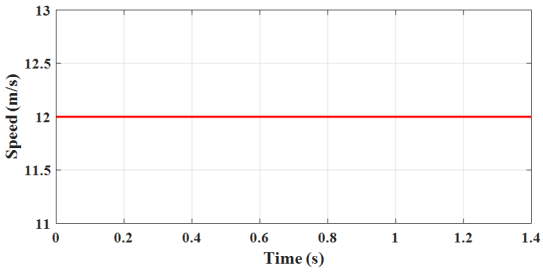

***Fig. 5**: Speed change analysis.*

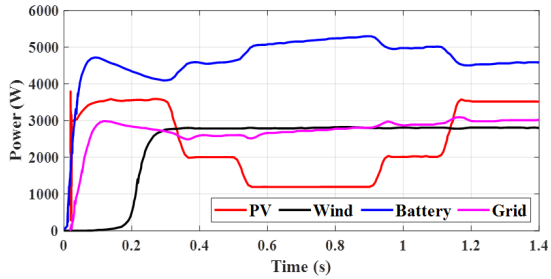

***Fig. 6**: Examination of the suggested individual power curve.*

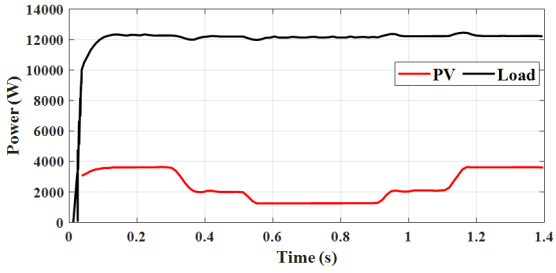

***Fig. 7**: PV analysis of the load's power curve.*

fluctuations. The grid power rises from 0 to around 2500 kW by 0.2 seconds, stabilizes around 2700 kW, and shows a small dip near 1.2 seconds before stabilizing again. These values highlight the interaction of different power sources to maintain balance in the hybrid system.

Fig. 7 illustrates the power behavior of a load and PV system during a change in irradiance for Case 1. The load power, represented by the upper curve, remains consistently around 12,000 W throughout the simulation period, indicating a stable load demand. The PV power

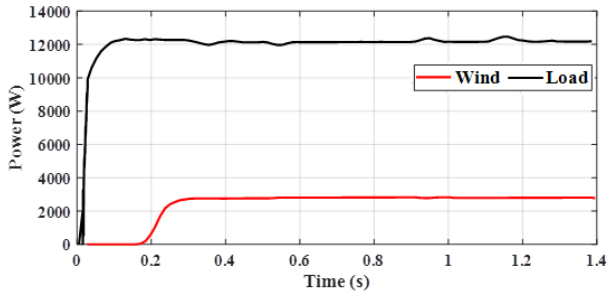

***Fig. 8**: Power curve analysis for a load with wind.*

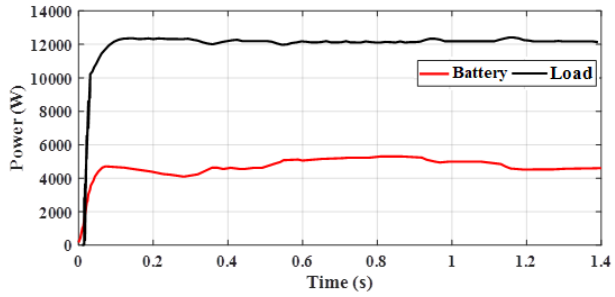

***Fig. 9**: Power curve analysis of a load using a battery.*

output, shown by the lower curve, initially rises to approximately 3,500 W at around 0.1 seconds. However, after 0.4 seconds, a decrease in irradiance causes the PV power to drop to about 2,000 W. This reduced output lasts until around 1.2 seconds, after which the PV power starts increasing again, returning to its original level of 3,500 W. The plot shows how the load power remains unaffected by the changes in irradiance, while the PV system dynamically adjusts according to the irradiance conditions. Fig. 8 illustrates the power output of wind energy and the load over time in Case 1, where a change in irradiance is considered. The wind power output starts at 0 W and rapidly rises to approximately 2000 W at around 0.2 seconds, after which it stabilizes with minor fluctuations throughout the simulation. The load power experiences a sharp increase and stabilizes at around 12000 W, also at approximately 0.2 seconds, maintaining this level for the remainder of the time (up to 1.4 seconds). This indicates that despite variations in irradiance, the system efficiently manages the load demand, with wind power contributing consistently. Fig. 9 presents the power output of the battery and the load over time in Case 1. The battery power initially spikes rapidly and stabilizes around 4000 W at 0.2 seconds. It fluctuates slightly throughout the simulation but maintains a relatively stable output. The load power similarly rises sharply, reaching approximately 12000 W at around 0.2 seconds, where it remains consistent for the rest of the period (up to 1.4 seconds). This behavior indicates that the battery is contributing to meeting the load demand, with both power sources stabilizing effectively after the initial surge.

Case 2: 3-phase load and irradiance change

In Fig. 10, the irradiance, measured in (W/m^2), is plotted against time (in seconds) for Case 2, where there is a change in irradiance along with a 3-phase load condition. Initially, the irradiance is steady at 1000 W/m^2 until around 0.65 seconds, after which a sharp decline is observed. The irradiance drops significantly and stabilizes at approximately 700 (W/m^2), indicating a sudden reduction in solar irradiance. This reduction likely reflects a change in environmental conditions, such as cloud cover or shading, which can affect the input power to the HRES. The system responds to this change and maintains the new irradiance level consistently after the drop, highlighting how fluctuations in irradiance impact the energy input in the system. Fig. 11 depicts the speed (measured in m/s) over time (in seconds) for Case 2, where changes in speed are analyzed. Throughout the entire time range (0 to 1.4 seconds), the speed remains constant at 12 m/s, indicating no noticeable variation in speed during this period. Despite potential changes in external conditions, such as irradiance (as seen in Fig. 10), the speed remains unaffected, suggesting that the system maintains consistent operational performance with respect to speed under these conditions. Fig. 12 shows the power contributions of different energy sources (PV, wind, battery, and grid) over time. Initially, PV power rises sharply to 3000 kW and remains stable until about 0.7 seconds, where it drops to 2000 kW due to a reduction in irradiance. Wind power quickly stabilizes at around 5000 kW, with minimal fluctuations, indicating a stable wind resource. The battery discharges initially, peaks at about 2000 kW during the irradiance drop around 0.7 seconds, and then stabilizes. The grid initially provides about 4000 kW, but its contribution decreases as other sources adjust, eventually stabilizing with slight fluctuations. This figure highlights the dynamic interplay between the energy sources to maintain system balance.

Fig. 13 shows the power curve for the PV system and the load in a case with a 3-phase load and an irradiation shift (Case 2). The PV power starts at approximately 4000 W and remains steady, for a short duration before experiencing fluctuations. Between 0.4 s and 0.8 s, the PV power output decreases to around 2500 W due to the change in irradiance, reflecting reduced solar energy input. After 1 s, the PV output increases again and stabilizes at about 4000 W. The load power begins at around 12000 W and remains relatively constant throughout the time interval, with minor variations. This stabilizing pattern demonstrates how load requirements remain steady yet the PV system responds to solar irradiation variations. The converter maintains load power delivery properly when adjusting to power variations, thus proving its capability in managing power changes. Fig. 14 shows the power curve for both the wind system and the load under conditions. Throughout the first 0.2 seconds, the wind power rises from an initial zero value before achieving its peak level of 2000 W. The wind power plant operates at its stable

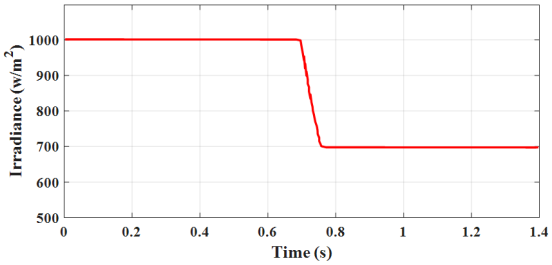

***Fig. 10**: Examination of the irradiance change.*

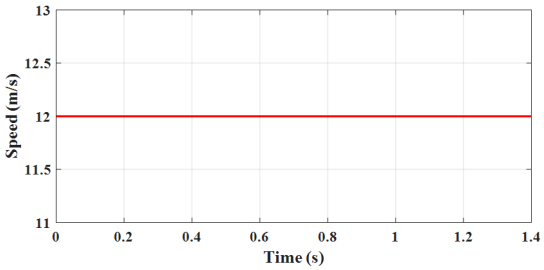

***Fig. 11**: Analysis of speed variation.*

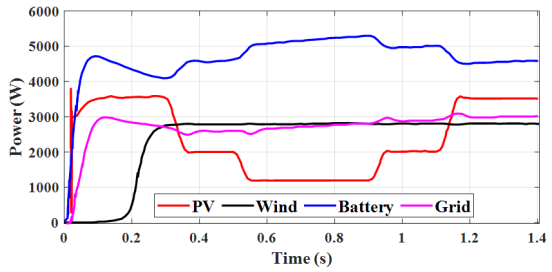

***Fig. 12**: Individual power curve analysis.*

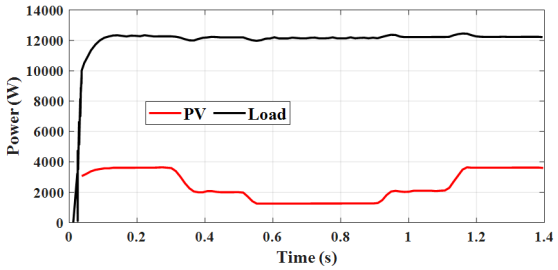

***Fig. 13**: PV analysis of the load's power curve.*

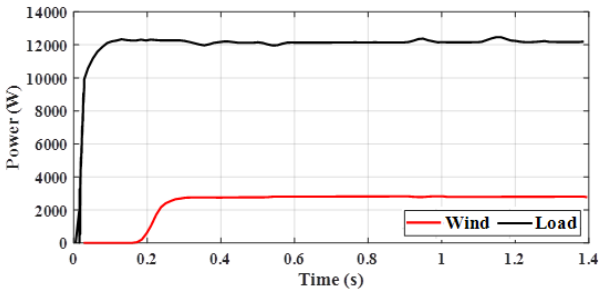

***Fig. 14**: Examination of the load's power curve with wind.*

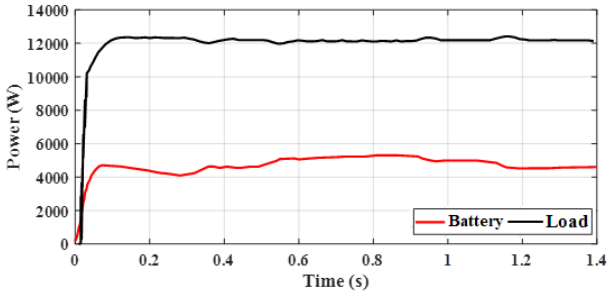

***Fig. 15**: Power curve analysis of a battery-powered load.*

operation state when the output reaches this level. The observed power output of the load remains at 12000 W until the conclusion of measurement time. As PV did previously, the load maintains its power demand level as wind power reaches stabilization following a quick adjustment phase. The system shows excellent dual functionality by merging wind power generation with constant load power delivery for uninterrupted load management. Fig. 15 represents the power curves between the battery systems together with the load during Case 2 of assessment. The starting battery power stands at 4000 W, which evens out to maintain this value before fluctuating minimally throughout the time span. During the observed period, the load power maintained its initial value of 12000 W before it showed some minor fluctuating variations. The battery operates with relative power consistency to back up load requirements, which stay unchanged. The figure demonstrates how the battery function ensures stable power delivery to the load by balancing its requirements and preventing supply disruptions from other power sources.

Case 3: 3-phase load fault with wind variation

Fig. 16 exhibits irradiance time analysis for Case 3. At approximately 1000 W/m² ,the irradiance stays constant from 0 to 1.4 seconds in the duration of the analysis. The stability of solar input remains consistent because no significant irradiance changes are detected between 0 and 1.4 seconds. The particular fault condition has no influence on the irradiance component of the hybrid system because of its stable performance. Fig. 17 shows the analysis of WS variation over time for Case 3. From the beginning of the measurement, the WS maintains a value of 12 m/s until the first 0.4 seconds pass. During the period of 0.4 to 0.6 seconds, the magnitude of WS reduces to 11 m/s. The speed records 8 m/s between time marks 0.6 to 0.8 seconds. The WS then recovers, increasing back to 11 m/s from 0.8 to 1 second, and finally, it returns to its initial value of 12 m/s from 1 to 1.4 seconds. This pattern reflects fluctuations in WS during the fault condition, potentially simulating variable wind conditions affecting system performance. Fig. 18 illustrates the power distribution among the PV system, load, battery, and grid for Case 3. The PV power initially rises to around 3500

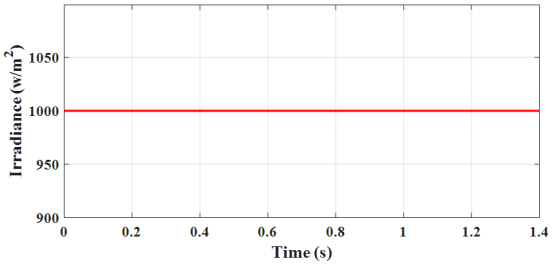

***Fig. 16**: Irradiance change analysis.*

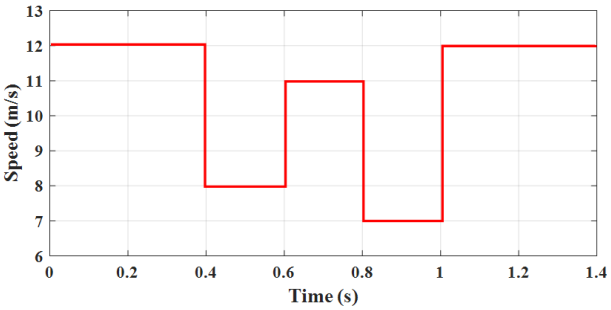

***Fig. 17**: Examination of velocity variation.*

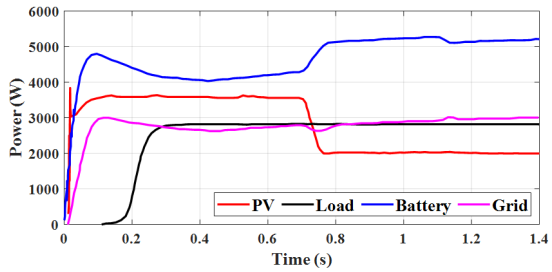

***Fig. 18**: Individual power curve analysis.*

***Table 3**: Efficiency comparison between suggested and existing approaches.*

Solution Techniques	Efficiency (%)
JS-RDF	73.5
INSGA-II	78.9
EA	81.2
PSO-LAPO	87.6
GSO	90.3
ARO-PHNN (proposed)	98.1

W and stabilizes until 0.8 seconds, after which it dips below 3000 W. The load power increases quickly to about 3500 W by 0.2 seconds, remaining stable throughout the time. The battery power spikes to over 5000 W around 0.2 seconds and fluctuates slightly, maintaining a level just below 5000 W. The grid power rises sharply from 1500 W to 3000 W at 0.2 seconds and stays stable with minor variations. These power levels reflect the system's adaptive response to changing wind conditions and load faults.

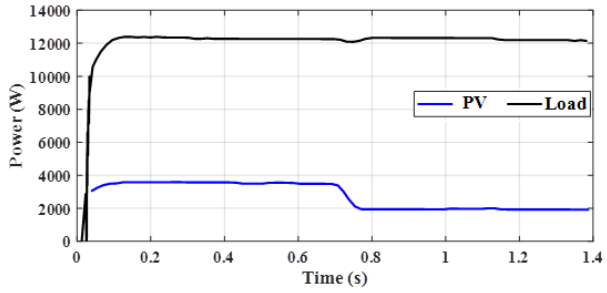

***Fig. 19**: PV analysis of the load's power curve.*

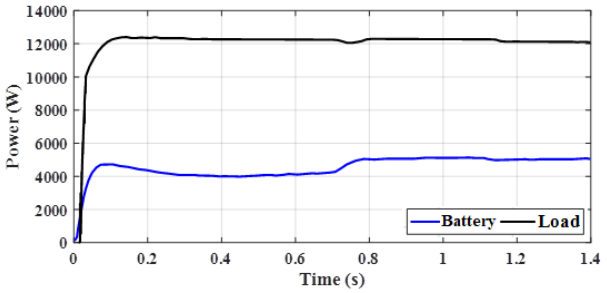

***Fig. 20**: Power curve analysis of a load using a battery.*

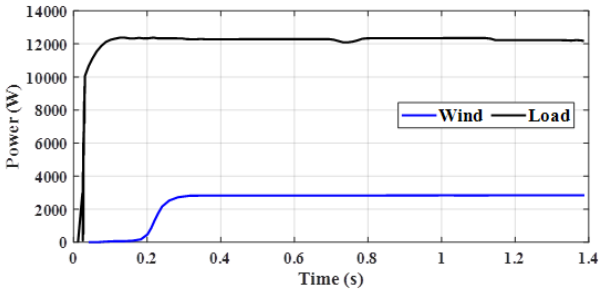

***Fig. 21**: Examination of the load's power curve with wind.*

***Table 4**: Statistical analysis comparison with proposed and existing methods.*

Methods	Mean	Median	SD
JS-RDF	1.5882	1.2941	0.1052
INSGA-II	1.2946	1.1653	0.0194
EA	1.0382	1.0039	0.0144
PSO-LAPO	0.9983	0.9672	0.0095
GSO	0.9890	0.9201	0.0078
ARO-PHNN (proposed)	0.9421	0.8612	0.0065

Fig. 19 shows the PV and load power curves over a 1.4-second period for Case 3, which includes a 3-phase load fault and a change in WS. Initially, the load power is around 12,000 W and remains relatively constant throughout the time. The PV power starts at approximately 4,000 W, staying steady until about 0.6 seconds, after which it drops due to the change in wind and the fault. By 0.8 seconds, the PV power decreases to around 2,500 W and stabilizes at that value for the

***Table 5**: Comparison of Simulated and Calculated Results for ARO-PHNN Method.*

Parameter	Simulated Value	Calculated Value
Efficiency (%)	98.1	96.5
Mean	0.9421	0.9500
Median	0.8612	0.8650
SD	0.0065	0.0067
Response Time (ms)	15.2	16.0

remainder of the period. Fig. 20 shows the power curve of both the battery and the load over 1.4 seconds for Case 3, which involves a change in wind and a 3-phase load fault. The load power remains stable at approximately 12,000 W throughout the time period. Initially, the battery power rises quickly to around 4,000 W, where it remains fairly constant until around 0.8 seconds. After this point, the battery power slightly increases to around 4,500 W and remains stable for the rest of the time period. This indicates that the battery compensates for the power drop in the system during the fault scenario. The power distribution of the wind source as well as the load for Case 3, which includes a shift in wind and a 3-phase load fault, is shown in Fig. 21 for a period of 1.4 seconds. The load power remains steady at approximately 12,000 W throughout the entire duration. The wind power starts near zero and increases rapidly, reaching around 2,500 W by 0.3 seconds. After this point, the wind power stabilizes and remains constant for the rest of the time period, indicating the wind source's contribution to maintaining system stability during the fault.

Table 3 compares the efficiency of various solution techniques, including the proposed ARO-PHNN method, with existing methods. The JS-RDF method achieves an efficiency of 73.5%, while INSGA-II improves upon this with 78.9%. EA further enhances efficiency, reaching 81.2%, and PSO-LAPO increases it to 87.6%. GSO performs even better, with an efficiency of 90.3%. The proposed ARO-PHNN method significantly outperforms all these techniques, achieving the highest efficiency at 98.1%. This illustrates the superior performance of the ARO-PHNN approach in comparison to other existing methods. Table 4 presents a statistical analysis comparing various methods, including the proposed ARO-PHNN, in terms of mean, median, and SD. The JS-RDF method has the highest mean (1.5882) and median (1.2941) with a relatively large SD (0.1052), indicating more variability. INSGA-II shows improvement with a lower mean (1.2946), median (1.1653), and reduced SD (0.0194). EA further reduces these values, with a mean of 1.0382, a median of 1.0039, and an SD of 0.0144. PSO-LAPO and GSO continue this trend, showing decreasing means and medians, with GSO having a mean of 0.9890 and an SD of 0.0078. The proposed ARO-PHNN method outperforms all others, having the lowest mean (0.9421), median (0.8612), and SD (0.0065), indicating not only higher accuracy but also more stability and consistency.

***Table 6**: Comparison of Advantages and Disadvantages of the Proposed Method with Existing Published Studies.*

Method	Advantages	Disadvantages
JS-RDF [16]	- Good for theoretical modeling and control pulse prediction. - High mean and median values, indicating a stable theoretical framework.	- Only 73.5% efficiency. - Exhibits inconsistency in results, especially in dynamic scenarios.
INSGA-II [19]	- Improved convergence rate over basic genetic algorithms. - Employs a multi-objective optimization approach.	- Efficiency at 78.9% is still below ARO-PHNN. - Can get stuck in local optima, limiting performance under varied conditions.
EA [20]	- Utilizes principles of natural selection, allowing for flexible behavior in optimization. - Operationally straightforward to implement.	- Efficiency of 81.2% shows improvements but lacks consistency due to stochasticity. - Lesser adaptability to rapidly changing conditions.
PSO-LAPO [21]	- Strong local search capabilities enhance outcomes in static scenarios. - More structured than traditional PSO approaches.	- Efficiency of 87.6% is commendable but can fluctuate based on environment. - Slower adjustments to rapid fluctuations in inputs.
GSO [22]	- Improved efficiency levels (90.3%) over conventional optimization techniques. - Consistent behavior under controlled scenarios.	- While better than some predecessors, GSO still may struggle with dynamic environmental changes. - Less effective under extreme conditions than ARO-PHNN.
ARO-PHNN (Proposed)	- Achieves 98.1%, outperforming all existing methods. - Low SD (0.0065) indicates consistent performance. - Validated against multiple existing techniques, showcasing clear benefits in responsiveness and reliability.	- May not be universally applicable to all converter topologies. - Requires advanced computational resources and expertise for real-world applications.

Table 5 compares simulated and calculated results for

the ARO-PHNN method, showing close agreement in efficiency, statistical metrics, and response time, with minor deviations. The simulated efficiency is slightly higher, while response time differences remain minimal.

4.1 Discussion

The discussion explores the dynamic behavior of HRES across various scenarios. In Case 1, a change in irradiance shows the system's ability to adapt to solar fluctuations, with PV power adjusting to irradiance levels while wind power and battery systems maintain stability. The load demand remains steady, indicating efficient load management. Case 2, which includes a 3-phase load, demonstrates the system's resilience, as the PV and wind power sources adjust to irradiance changes while maintaining load stability. The battery plays a crucial role in compensating for fluctuations. Case 3 introduces wind variation and a load fault scenario, where the wind power shows variability, but the system remains balanced due to the adaptive responses of PV, battery, and grid systems. Across all cases, the hybrid system efficiently manages power distribution despite environmental changes, with the proposed ARO-PHNN method achieving the highest efficiency of 98.1%. Additionally, it demonstrates superior stability with a mean value of 0.9421, a median of 0.8612, and a low SD of 0.0065, reflecting its accuracy and consistency in comparison to other methods. Table 6 shows the comparison of advantages and disadvantages of the proposed method with existing published studies.

5. CONCLUSION

In conclusion, the suggested ARO-PHNN method represents a significant advancement in the optimization of DC-DC converters for HRES. The suggested ARO-PHNN method significantly advances the optimization of DC-DC converters in HRES, achieving an impressive efficiency of 98.1%. This hybrid approach, which integrates ARO and PHNN, simplifies the complexities of converter design while enhancing power efficiency. The method demonstrates high accuracy, with a mean value of 0.9421 and a low SD of 0.0065, indicating stability and reliability. The evaluation against existing methods further highlights the ARO-PHNN technique's effectiveness in improving EM and system performance, paving the way for future advancements in the field. One limitation of the ARO-PHNN method is its reliance on specific algorithms that may not be universally applicable across all types of DC-DC converter topologies. Additionally, the complexity of implementing the hybrid approach may pose challenges in real-world applications, potentially requiring advanced computational resources and expertise. Future work could focus on extending the proposed hybrid optimization approach to other energy conversion systems, such as AC-DC converters, to evaluate its broader applicability. Additionally, incorporating real-time adaptive learning and hardware-in-the-loop simulations could enhance practical implementation and performance in dynamic environments.

REFERENCES

[1] A. Zakaria, M. I. Marei, H. M. Mashaly, "A Hybrid Interleaved DC-DC Converter Based on Buck-Boost topologies for Medium Voltage Applications," *E-Prime-Advances in Electrical Engineering, Electronics and Energy*, Vol. 6, p. 100301, 2023.

[2] Y. Yasa, "A system efficiency improvement of DC fast-chargers in electric vehicle applications: Bypassing second-stage full-bridge DC-DC converter in high-voltage charging levels," *Ain Shams Engineering Journal*, Vol. 14, no. 9, p. 102391, 2023.

[3] A. Raj, R. P. Praveen, "Highly efficient DC-DC boost converter implemented with improved MPPT algorithm for utility level photovoltaic applications," *Ain Shams Engineering Journal,* Vol. 13, no. 3, p. 101617, 2022.

[4] K. Osmani, A. Haddad, T. Lemenand, B. Castanier, M. Ramadan, "An investigation on maximum power extraction algorithms from PV systems with corresponding DC-DC converters," *Energy*, Vol. 224, p. 120092, 2021.

[5] R. Aravind, C. Bharatiraja, R. Verma, S. Aruchamy, L. Mihet-Popa, "Multi-port non-isolated DC-DC converters and their control techniques for the applications of renewable energy," *IEEE Access*. 2024.

[6] J. Wang, R. Peng, C. Cai, Yu, H., Chen, M., Y. Liu, J. Chen, "An efficiency optimization control method for three-phase interleaved dc-dc converter," *In 2021 3rd Asia Energy and Electrical Engineering Symposium (AEEES)* 2021 (pp. 285-289). IEEE.

[7] P. Gunawardena, N. Hou, D. Nayanasiri, Y. Li, "A dual-input single-output DC-DC converter topology for renewable energy applications," *IEEE Transactions on Industry Applications*, Vol. 59, no. 2, pp. 1995-2006, 2022.

[8] H. Nguyen, W. Jung, "ConverGenT: Automated topology generation and analysis of hybrid DC–DC converters," *IEEE Transactions on Power Electronics*, Vol. 38, no. 9, pp. 11193-11220, 2023.

[9] I. N. Jiya, A. Salem, Van Khang, H., R. Pomarnacki, "Integrated Multiport DC-DC and Multilevel Converters for Multiple Renewable Energy Source Integration," *IEEE Access*, Vol. 11, pp. 132483-132495, 2023.

[10] K. Suriyan, P., K, K. S. M. C, M. Adhikary, M. CS, B. N. K, "A novel reconfigurable hybrid DC-AC home technique with renewable energy resources and converters," *International Journal of Sustainable Engineering*, Vol. 16, no. 1, pp. 285-301, 2023.

[11] F. Jin, A. Nabih, T. Yuan, Q. Li, "A High Efficiency High Density Three-Phase CLLC Resonant Converter With a Universally Derived Three-Phase Integrated Transformer for On-Board Charger Ap-

plication," *IEEE Transactions on Power Electronics*. 2024.

[12] S. Rafikiran, G. Devadasu, C. H. Basha, P. M. Tom, V. Prashanth, Dhanamjayulu, C. S. M.. Muyeen, "Design and performance analysis of hybrid MPPT controllers for fuel cell fed DC-DC converter systems," *Energy Reports*, Vol. 9, pp. 5826-584, 22023.

[13] M. L. Alghaythi, "A Non-Isolated High Voltage Gain DC–DC Converter Suitable for Sustainable Energy Systems," *Sustainability*, Vol. 15, no. 15, p. 12058, 2023.

[14] A. P. Mohamed, K. V. Chandrakala, Balamurugan, S., U. Subramaniam, D. Almakhles, (2024). "Adaptive maximum power extraction technique in fuel-cell integrated with novel DC-DC converter topology for low-power electric vehicle applications," *Engineering Science and Technology, an International Journal*, Vol. 54, p. 101723.

[15] W. Hu, F. Li, "Improved Topology and Control Strategies for DC Converters in Wind Power Full DC Systems," *Electronics*, Vol. 13, no. 2, p. 400, 2024.

[16] N. Karthikeyan, G. A. Jebaselvi, "A bidirectional four-port DC–DC converter for grid connected and isolated loads of hybrid renewable energy system using hybrid approach," *Analog Integrated Circuits and Signal Processing*, Vol. 118, no. 3, pp. 467-487, 2024.

[17] S. Hasanpour, T. Nouri, M. Shaneh, "Analysis and design of a new ultra-step-up DC–DC converter with reduced voltage stress for renewable energy systems applications," *Iranian Journal of Science and Technology, Transactions of Electrical Engineering*, Vol. 48, no. 2, pp. 817-830, 2024.

[18] H. Meshael, A. Elkhateb, R. Best, "Topologies and design characteristics of isolated high step-up DC–DC converters for photovoltaic systems," *Electronics*, Vol. 12, no. 18, p. 3913, 2023.

[19] S. Rajasekaran, S. Suresh, Ramkumar, A., K. Karthikeyan, "A novel solar photovoltaic integrated modified SEPIC high gain DC–DC converter using evolutionary algorithms for electric vehicle battery applications," *Journal of Electrical Engineering & Technology*, Vol. 18, no. 5, pp. 3681-3694, 2023.

[20] E. Mendez-Flores, A. Ortiz, I. Macias, A. Molina, "Experimental validation of an enhanced MPPT algorithm and an optimal DC–DC converter design powered by metaheuristic optimization for PV systems," *Energies*, Vol. 15, no. 21, p. 8043, 2022.

[21] B. Saleh, A. M. Yousef, M. Ebeed, F. K. Abo-Elyousr, A. Elnozahy, M. Mohamed, and S. A. M. Abdelwahab, Design of PID controller with grid connected hybrid renewable energy system using optimization algorithms," *Journal of Electrical Engineering & Technology*, Vol. 16, no. 6, pp. 3219-3233, 2021.

[22] R. Rajasekaran, P. U. Rani, "Bidirectional DC-DC converter for microgrid in energy management system," *International Journal of Electronics*, Vol. 108, no. 2, pp. 322-343, 2021.

[23] D. Tamilselvan, T. D. Sudhakar, "Optimizing renewable energy utilization with high gain converters," *Renewable and Sustainable Energy Reviews*, Vol. 191, p. 114105, 2024.

[24] D. Yousri, T. S. Babu, E. Beshr, Eteiba, M. B., D. Allam, "A robust strategy based on marine predators algorithm for large scale photovoltaic array reconfiguration to mitigate the partial shading effect on the performance of PV system," *IEEE Access*, Vol. 8, pp. 112407-112426, 2020.

[25] H. Armghan, M. Yang, Armghan, A., N. Ali, M. Q. Wang, I. Ahmad, "Design of integral terminal sliding mode controller for the hybrid AC/DC microgrids involving renewables and energy storage systems," *International Journal of Electrical Power & Energy Systems*, Vol. 119, p. 105857, 2020.

[26] L. Wang, Q. Cao, Z. Zhang, S. Mirjalili, W. Zhao, "Artificial rabbits optimization: A new bio-inspired meta-heuristic algorithm for solving engineering optimization problems," *Engineering Applications of Artificial Intelligence*, Vol. 114, p. 105082 2022.

[27] S. Eidnes, A.J. Stasik, C. Sterud, E. Bøhn, and S. Riemer-Sørensen, "Pseudo- Hamiltonian neural networks with state-dependent external forces," *Physica D: Nonlinear Phenomena*, Vol. 446, pp. 133673, 2023.